Vortex electron energy loss spectroscopy for near-field mapping of magnetic plasmons

Zeinab Mohammadi, Cope P. Van Vlack, Stephen Hughes, Jens Bornemann, and Reuven Gordon

2012

This article was originally published at: https://doi.org/10.1364/OE.20.015024

Vortex electron energy loss spectroscopy for near-field mapping of magnetic plasmons

Zeinab Mohammadi,[1] **Cole P. Van Vlack,**[2] **Stephen Hughes,**[2] **Jens Bornemann,**[1] **and Reuven Gordon**[1,*]

[1]*Department of Electrical and Computer Engineering, University of Victoria, Victoria, BC, V8P 5C2 Canada*

[2]*Department of Physics, Queen's University, Kingston, Ontario, K7L 3N6 Canada*

[*]*rgordon@uvic.ca*

Abstract: The theory of vortex electron beam electron energy loss spectroscopy (EELS), or vortex-EELS for short, is presented. This theory is applied, using Green function calculations within the finite-difference time-domain method, to calculate spatially resolved vortex-EELS maps of a metal split ring resonator (SRR). The vortex-EELS scattering cross section for the SRR structure is within an order of magnitude of conventional EELS typically for metal nanoparticles. This is promising in terms of feasibility for future measurements to map out the local magnetic response of metal nanostructures and to characterize their magnetic plasmon response in applications, including metamaterials.

OCIS codes: (240.6680) Surface plasmons; (160.3918) Metamaterials; (300.6330) Spectroscopy, inelastic scattering including Raman.

References and links

1. L. D. Landau, L. P. Pitaevskii, and E. M. Lifshitz, *Electrodynamics of Continuous Media* **8**, (Pergamon Press, 1984).
2. W. Cai, U. K. Chettiar, A. V. Kildishev, and V. M. Shalaev, "Optical cloaking with metamaterials," Nat. Photonics **1**, 224–227 (2007).
3. A. Alu and N. Engheta, "Cloaking and transparency for collections of particles with metamaterial and plasmonic covers," Opt. Express **15**, 7578–7590 (2007).
4. B. Kanté, A. de Lustrac, J. M. Lourtioz, and S. N. Burokur, "Infrared cloaking based on the electric response of split ring resonators," Opt. Express **16**, 9191–9198 (2008).
5. D. R. Smith, J. B. Pendry, and M. C. K. Wiltshire, "Metamaterials and negative refractive index," Science **305**, 788–792 (2004).
6. V. M. Shalaev, W. Cai, U. K. Chettiar, H. K. Yuan, A. K. Sarychev, V. P. Drachev, and A. V. Kildishev, "Negative index of refraction in optical metamaterials," Opt. Lett. **30**, 3356–3358 (2005).
7. R. Merlin, "Metamaterials and the Landau-Lifshitz permeability argument: Large permittivity begets high-frequency magnetism," Proc. Natl. Acad. Sci. U.S.A. **106**, 1693–1698 (2009).
8. V. M. Shalaev, "Optical negative-index metamaterials," Nat. Photonics **1**, 41–48 (2007).
9. R. Marqués, J. Martel, F. Mesa, and F. Medina, "Left-handed-media simulation and transmission of EM waves in subwavelength split-ring-resonator-loaded metallic waveguides," Phys. Rev. Lett. **89**, 183901 (2002).
10. A. Alu and N. Engheta, "The quest for magnetic plasmons at optical frequencies," Opt. Express **17**, 5723–5730 (2009).
11. A. K. Sarychev, G. Shvets, and V. M. Shalaev, "Magnetic plasmon resonance," Phys. Rev. E **73**, 036609 (2006).
12. S. Linden, C. Enkrich, M. Wegener, J. Zhou, T. Koschny, and C. M. Soukoulis, "Magnetic response of metamaterials at 100 terahertz," Science **306**, 1351–1353 (2004).

#166622 - $15.00 USD Received 13 Apr 2012; revised 25 May 2012; accepted 11 Jun 2012; published 20 Jun 2012

13. A. N. Grigorenko, H. F. Gleeson, Y. Zhang, A. A. Firsov, I. Y. Khrushchev, and J. Petrovic, "Nanofabricated media with negative permeability at visible frequencies," Nature **438**, 335 (2005).
14. C. Enkrich, M. Wegener, S. Linden, S. Burger, L. Zschiedrich, F. Schmidt, J. F. Zhou, T. Koschny, and C. M. Soukoulis, "Magnetic metamaterials at telecommunication and visible frequencies," Phys. Rev. Lett. **95**, 203901 (2005).
15. A. W. Blackstock, R. H. Ritchie, and R. D. Birkhoff, "Mean free path for discrete electron energy losses in metallic foils," Phys. Rev. **100**, 1078–1083 (1955).
16. E. A. Stern and R. A. Ferrell, "Surface plasma oscillations of a degenerate electron gas," Phys. Rev. **120**, 130–136 (1960).
17. P. Batson, "Inelastic scattering of fast electrons in clusters of small spheres," Surf. Sci. **156**, 720–734 (1985).
18. F. J. García de Abajo and A. Howie, "Relativistic electron energy loss and electron-induced photon emission in inhomogeneous dielectrics," Phys. Rev. Lett. **80**, 5180–5183 (1998).
19. R. Vincent and J. Silcox, "Dispersion of radiative surface plasmons in aluminum films by electron scattering," Phys. Rev. Lett. **31**, 1487–1490 (1973).
20. R. B. Pettit, J. Silcox, and R. Vincent, "Measurement of surface-plasmon dispersion in oxidized aluminum films," Phys. Rev. B **11**, 3116–3123 (1975).
21. H. A. Brink, M. M. G. Barfels, R. P. Burgner, and B. N. Edwards, "A sub-50 meV spectrometer and energy filter for use in combination with 200 kv monochromated TEMs," Ultramicroscopy **96**, 367–384 (2003).
22. B. Schaffer, U. Hohenester, A. Trügler, and F. Hofer, "High-resolution surface plasmon imaging of gold nanoparticles by energy-filtered transmission electron microscopy," Phys. Rev. B **79**, 041401 (2009).
23. W. Zhong, J. Xu, and X. Zhang, "Interaction of fast electron beam with photonic quasicrystals," Opt. Express **17**, 13270–13282 (2009).
24. U. Hohenester, H. Ditlbacher, and J. R. Krenn, "Electron-energy-loss spectra of plasmonic nanoparticles," Phys. Rev. Lett. **103**, 106801 (2009).
25. M. NǴom, S. Li, G. Schatz, R. Erni, A. Agarwal, N. Kotov, and T. B. Norris, "Electron-beam mapping of plasmon resonances in electromagnetically interacting gold nanorods," Phys. Rev. B **80**, 113411 (2009).
26. F. J. García de Abajo, "Optical excitations in electron microscopy," Rev. Mod. Phys. **82**, 209–275 (2010).
27. A. L. Koh, A. I. Fernández-Domínguez, D. W. McComb, S. A. Maier, and J. K. W. Yang, "High-resolution mapping of electron-beam-excited plasmon modes in lithographically defined gold nanostructures," Nano Lett. **11**, 1323–1330 (2011).
28. M. W. Chu, V. Myroshnychenko, C. Chen, J. P. Deng, C. Y. Mou, and F. J. García de Abajo, "Probing bright and dark surface-plasmon modes in individual and coupled nobel metal nanoparticles using an electron beam," Nano Lett. **1**, 399–404 (2009).
29. M. Uchida and A. Tonomura, "Generatio of electron beams carrying orbital angular momentum," Nature **464**, 737–739 (2010).
30. J. Verbeeck, H. Tian, and P. Schattschneider, "Production and application of electron vortex beams," Nature **467**, 301–304 (2010).
31. K. Y. Bliokh, Y. P. Bliokh, S. Savelév, and F. Nori, "Semiclassical dynamics of electron wave packet states with phase vortices," Phys. Rev. Lett. **99**, 190404 (2007).
32. B. Thidé, H. Then, J. Sjöholm, K. Palmer, J. Bergman, T. D. Carozzi, Y. N. Istomin, N. H. Ibragimov, and R. Khamitova, "Utilization of photon orbital angular momentum in the low-frequency radio domain," Phys. Rev. Lett. **99**, 087701 (2007).
33. F. J. García de Abajo and M. Kociak, "Probing the photonic local density of states with electron energy loss spectroscopy," Phys. Rev. Lett. **100**, 106804 (2008).
34. P. E. Mayes, "The equivalence of electric and magnetic sources," IEEE Trans. Antennas Propag. **6**, 295–296 (1958).
35. J. D. Jackson, *Classical Electrodynamics* (Wiley, 1999).
36. P. Schattschneider and J. Verbeeck, "Theory of free electron vortices," Ultramicroscopy **111**, 1461–1468 (2011).
37. F. J. García de Abajo, "Optical excitations in electron microscopy," Rev. Mod. Phys. **82**, 209–275 (2010).
38. P. B. Johnson and R. W. Christy, "Optical constants of the noble metals," Phys. Rev. B **6**, 4370–4379 (1972).
39. C. P. Van Vlack and S. Hughes, "Finite-difference time domain technique as an efficient tool for obtaining the regularized green function: applications to the local field problem in quantum optics for inhomogeneous lossy materials," Opt. Lett. (submitted) (2012).
40. B. J. McMorran, A. Agrawal, I. M. Anderson, A. A. Herzing, H. J. Lezec, J. J. McClelland, and J. Unguris, "Electron vortex beams with high quanta of orbital angular momentum," Science **331**, 192–195 (2011).
41. R. F. Egerton, *Electron Energy loss Spectroscopy in the Electron Microscope* (Springer, 2011).
42. G. Boudarham, N. Feth, V. Myroshnychenko, S. Linden, F. J. García de Abajo, M. Wegener, and M. Kociak, "Spectral imaging of individual split-ring resonators," Phys. Rev. Lett. **105**, 255501 (2010).
43. C. Rockstuhl, F. Lederer, C. Etrich, S. Linden, T. Zentgraf, J. Kuhl, and H. Giessen, "On the reinterpretation of resonances in split-ring-resonators at normal incidence," Opt. Express **14**, 8827–8836 (2006).
44. K. Joulain, R. Carminati, J. P. Mulet, and J. J. Greffet, "Definition and measurement of the local density of electromagnetic states close to an interface," Phys. Rev. B **68**, 245405 (2003).

#166622 - $15.00 USD Received 13 Apr 2012; revised 25 May 2012; accepted 11 Jun 2012; published 20 Jun 2012

45. P. Schattschneider, M. Stöger-Pollach, S. Löffler, A. Steiger-Thirsfeld, J. Hell, and J. Verbeeck, "Sub-nanometer free electrons with topological charge," Ultramicroscopy **115**, 21–25 (2012).

1. Introduction

The magnetic response of naturally occurring materials is negligible in the visible-IR regime for fundamental reasons [1]. This severely limits the functionality of optics in that regime: were a strong magnetic response possible, many applications, such as optical cloaking [2–4] and perfect lensing [5, 6], could be achievable. It is possible to make the magnetic response stronger by using artificial metal nanostructures [7–11]. While great strides have been made towards achieving a stronger magnetic response in the visible regime [12–14], still further work is required to reduce the resonance wavelength, to increase the strength of the response and to reduce material losses. To aid in this continuing effort, it is highly desirable to have a tool to probe the magnetic response of metal nanostructures at the nanometer scale.

Electron energy loss spectroscopy (EELS) has long been used to probe the response of matter [15–18]. For example, the experimental measurement of a surface plasmon is commonly performed by EELS [19–21]. More recently, EELS has allowed for mapping out the electronic response of metal nanostructures, allowing for the probing of the distribution of localized surface plasmons [22–27]. Of particular interest, EELS can probe dark modes that are not coupled to radiation and cannot be measured with conventional methods [28].

Here, we propose using the well-established tool of electron energy loss scattering, but with the twist of vortex electron beams, or vortex-EELS, to map out the *magnetic* response of materials at the nanometer scale. Vortex electron beams have recently been demonstrated using diffractive phase-plates in transmission electron microscope setups [29, 30]. These electron beams possess orbital angular momentum (OAM), which has proven to be extremely useful in the field of optics [31, 32].

In this work, we show that these vortex electron beams provide an opportunity for mapping out the near-field magnetic response of metal nanostructures. First we present a semi-classical theory that shows how the spiraling electron trajectory creates a moving effective magnetic charge, which in turn can be used to probe the magnetic response of metal nanostructures at the nanometer scale. We present example calculations for the well-known split ring resonator (SRR) metal nanostructure, which show that the scattering signal achieved from vortex-EELS is within an order of magnitude of conventional EELS. These findings are extremely promising for future work to map out the local magnetic response at the nanometer scale.

2. Vortex-EELS Theory

The vortex-EELS theory is similar to past approaches to EELS that consider the energy loss from a moving point electron charge [33], except that here we consider a spiraling trajectory. This spiraling trajectory creates a magnetic current, that can be thought of as arising from a moving magnetic charge. Here we show how the magnetic charge and magnetic current density is related to the angular momentum and the trajectory of the electron beam. We then show how the energy loss spectrum can be obtained from the magnetic Green function that is induced from the magnetic charge.

2.1. Effective Magnetic Charge

The electron spiral has radius of a, while moving with constant velocity in the z-direction of v_z. The total electron velocity is

$$\boldsymbol{v} = -v_\theta \frac{y}{a}\hat{x} + v_\theta \frac{x}{a}\hat{y} + v_z\hat{z}, \tag{1}$$

#166622 - $15.00 USD Received 13 Apr 2012; revised 25 May 2012; accepted 11 Jun 2012; published 20 Jun 2012

where $\hat{x}$ is the x-directed unit vector. The electron current density is given by:

$$\boldsymbol{j}_e(\boldsymbol{r},t) = -e\delta\left[\boldsymbol{r}-\boldsymbol{r}_e(t)\right]\boldsymbol{v}, \tag{2}$$

where e is the magnitude of the electron unit charge, $\boldsymbol{r}_e(t)$ is the electron position as function of time and δ is the Dirac delta function. The magnetic current density is given by

$$\boldsymbol{j}_m(\boldsymbol{r},\omega) = \frac{-i}{\omega\varepsilon_0}\nabla\times\frac{1}{\boldsymbol{\varepsilon}_r(\boldsymbol{r},\omega)}\boldsymbol{j}_e(\boldsymbol{r},\omega), \tag{3}$$

where $i=\sqrt{-1}$ and ω is the angular frequency of the spiral. ε_0 and $\boldsymbol{\varepsilon}_r(\boldsymbol{r},\omega)$ are the free-space and relative permittivities, respectively. Further description about the origin of this equation is given in the Appendix and the free space version is discussed elsewhere [34]. The electric current has angular momentum along z axis, so that

$$(\nabla\times\boldsymbol{v})\cdot\hat{z} = \frac{2}{a}v_\theta. \tag{4}$$

To find v_θ, we use the angular momentum given by

$$L_z = mav_\theta, \tag{5}$$

where m is the electron mass. In addition, we use the fact that the vortex beam has quantized orbital angular momentum given by

$$L_z = n\hbar, \tag{6}$$

where n is the quantum number and $\hbar$ is the reduced Planck's constant. Combining these two equations for the angular momentum gives

$$v_\theta = \frac{n\hbar}{ma}. \tag{7}$$

We find the magnitude of the effective magnetic charge, e_m, by writing the magnetic charge density along z axis as follows:

$$e_m\delta\left[\boldsymbol{r}-\boldsymbol{r}_e(t)\right] = \frac{j_{mz}}{v_z} = \frac{2e}{a\omega\varepsilon}\frac{v_\theta}{v_z}\delta\left[\boldsymbol{r}-\boldsymbol{r}_e(t)\right], \tag{8}$$

where $\varepsilon=\varepsilon_0\varepsilon_r$ assuming ε_r is scalar and $j_{mz}=j_{mz}(\boldsymbol{r},t)$ is the z component of magnetic current. Subsequently, we obtain the effective magnetic charge:

$$e_m = \frac{2en\hbar}{m\omega\varepsilon v_z a^2}. \tag{9}$$

2.2. Vortex-EELS Scattering Loss Probability

The two differences between the present vortex-EELS theory and the conventional EELS theory are that: 1) the effective magnetic charge replaces the electric charge, and 2) the duality of the electric and the magnetic fields allows any calculation involving electric fields, permittivities and electric field Green functions to be replaced with magnetic fields, permeabilities and magnetic Green functions. The energy loss, ΔE, from a scattering object can be found from the Poynting theorem in the usual way [35], allowing for the inclusion of magnetic current:

$$\Delta E = \int \boldsymbol{j}_m\cdot\boldsymbol{H}^{\mathrm{ind}}dt = \int_0^\infty \hbar\omega\, d\omega\Gamma(\omega) \tag{10}$$

#166622 - $15.00 USD Received 13 Apr 2012; revised 25 May 2012; accepted 11 Jun 2012; published 20 Jun 2012

where $\boldsymbol{H}^{\mathrm{ind}}$ is the *induced* magnetic field from current source and $\Gamma(\omega)$ is the inelastic scattering probability. Here we use a semi-classical theory that considers a spiral electron particle motion with quantized angular momentum. We neglect energy loss that would typically result from the classical description of a spiraling electron beam. A quantum treatment of free electron vortices has been presented elsewhere [36]. A full quantum model for the electron trajectory, while interesting, is outside the scope of this first prediction. Past works on EELS have suggested that the quantum treatment only slightly modifies the quantitative predictions by weighting with the electron wavefunction magnitude squared [37].
Inserting for $\boldsymbol{j}_m(\boldsymbol{r},t)$ into Eq. (10), we have

$$\Delta E = e_m v_z \int H^{\mathrm{ind}} dt = \int_0^\infty \hbar\omega \, d\omega \Gamma(\omega). \tag{11}$$

The Fourier transform then gives

$$\boldsymbol{H}^{\mathrm{ind}}(\boldsymbol{r},t) = \frac{1}{2\pi}\int d\omega e^{-i\omega t}\boldsymbol{H}^{\mathrm{ind}}(\boldsymbol{r},\omega), \tag{12}$$

where the property $\boldsymbol{H}^{\mathrm{ind}}(\boldsymbol{r},\omega) = [\boldsymbol{H}^{\mathrm{ind}}(\boldsymbol{r},-\omega)]^*$ has been used. From this, we find the inelastic scattering probability, through

$$\Gamma(\omega) = \frac{e_m}{\pi\hbar\omega}\int dt\, \Im\left\{e^{-i\omega t} v_z H^{\mathrm{ind}}\left[\boldsymbol{r}_e(t),\omega\right]\right\} \tag{13}$$

where $\Im$ indicates the imaginary part.

The magnetic field can be obtained from the magnetic Green function (or tensor), $\overline{\boldsymbol{G}}^{\mathrm{H}}$, through

$$\boldsymbol{H}(\boldsymbol{r},\omega) = -i\omega\varepsilon_0 \int d\boldsymbol{r}' \overline{\boldsymbol{G}}^{\mathrm{H}}(\boldsymbol{r},\boldsymbol{r}',\omega)\cdot \boldsymbol{j}_m(\boldsymbol{r}',\omega). \tag{14}$$

Combining this with Eq. (13) and Eq. (8), we find the scattering probability for a given transverse coordinate $\boldsymbol{R}_0 = (x_0, y_0)$:

$$\Gamma(\boldsymbol{R}_0,\omega) = -\frac{e_m^2 v_z^2 \varepsilon_0}{\pi\hbar}\int dt dt' \,\Im\left\{e^{i\omega(t'-t)} G_{zz}^{\mathrm{H,ind}}[\boldsymbol{r}_e(t),\boldsymbol{r}_e(t'),\omega]\right\}, \tag{15}$$

where $G_{zz}^{\mathrm{H,ind}} = \hat{z}\cdot\overline{G}^{\mathrm{H,ind}}\cdot\hat{z}$; note that the dependence of the loss probability Γ on $\boldsymbol{R}_0$ is shown explicitly, and $G^{\mathrm{H,ind}}$ denotes the induced Green-tensor component obtained by subtracting the free-space Green green function. The Green function is defined in terms of the wave equation with a delta function excitation:

$$\nabla\times\frac{1}{\boldsymbol{\varepsilon}_r(\boldsymbol{r},\omega)}\nabla\times\overline{\boldsymbol{G}}^{\mathrm{H}}(\boldsymbol{r},\boldsymbol{r}',\omega) - \frac{\omega^2}{c^2}\overline{\boldsymbol{G}}^{\mathrm{H}}(\boldsymbol{r},\boldsymbol{r}',\omega) = \delta(\boldsymbol{r}-\boldsymbol{r}')\overline{\boldsymbol{I}}, \tag{16}$$

where $\overline{\boldsymbol{I}}$ is the unit tensor. This wave equation is derived from the fully vectorial Maxwell equations, and the corresponding boundary conditions are those of Maxwell equations for an outgoing wave, for which the Green function goes to zero at infinity. In practice, we calculate the Green function using numerical computation of the comprehensive Maxwell equations with a magnetic dipole source in the next section.

Noticing that $z_e(t) = v_z t$, the time integral of Eq. (15) can be expressed as an integral along magnetic charge trajectory, through

$$\Gamma(\boldsymbol{R}_0,\omega) = -\frac{e_m^2\varepsilon_0}{\pi\hbar}\int dz dz' \,\Im\left\{e^{i\omega(z'-z)/v_z} G_{zz}^{\mathrm{H,ind}}[(\boldsymbol{R}_0,z),(\boldsymbol{R}_0,z'),\omega]\right\}. \tag{17}$$

#166622 - $15.00 USD Received 13 Apr 2012; revised 25 May 2012; accepted 11 Jun 2012; published 20 Jun 2012

Equation (17) is the desired result for our calculations. It remains to calculate the Green function component G_{zz} for all positions along the trajectory of the magnetic charge produced by the vortex electron beam to calculate the vortex-EELS scattering probability. We will do this using finite-difference time-domain (FDTD) techniques, discussed below.

3. Vortex-EELS for a Split Ring Resonator using FDTD

To quantify the vortex-EELS probability for a nanometric structure, we consider a U-shaped SRR. Figure 1 shows a schematic of the SRR under consideration. The dimensions shown are chosen to match a past work [14].

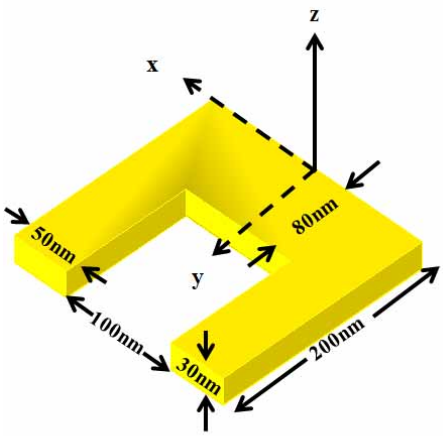

Fig. 1. Schematic of U-shaped split ring resonator showing dimensions and axes.

3.1. *FDTD Analysis of the SRR*

Figure 2 shows transmission and reflection of an array of the SRRs (see Fig. 1), with periodicity 315 nm along the *x*-direction and 330 nm along the *y*-direction. The transmission and reflection was calculated using FDTD simulations with a normally-incident plane wave source of *x*-polarization. The response of gold is taken from experiments [38]. We use a uniform grid around the nanostructure with mesh size 4 nm in all directions, Bloch boundaries in the *x*- and *y*-directions and perfectly matched layer boundaries in the positive and negative *z*-direction. Figure 2 agrees quantitatively with past calculations using the finite element calculation method for the same structure [14].

3.2. *Vortex-EELS Maps for the SRR*

Figure 3 shows the vortex-EELS scattering probability for a 100 keV beam with $\boldsymbol{R}_0 = (0, 90\text{ nm})$, as calculated using Eq. (17). The Green tensor component, G_{zz}^{ind}, was calculated using a *z*-oriented magnetic dipole source in FDTD with perfectly matched layer boundary conditions, and monitoring the *z* component of the magnetic field. Simulations were carried out for 30 positions of the magnetic dipole source positions with a 4 nm spacing. For dipoles within the lossy material, FDTD properly accounts for regularization of the Green tensor [39]. The radius of the vortex beam is taken to be 1 nm, which has been shown in recent experi-

#166622 - $15.00 USD Received 13 Apr 2012; revised 25 May 2012; accepted 11 Jun 2012; published 20 Jun 2012

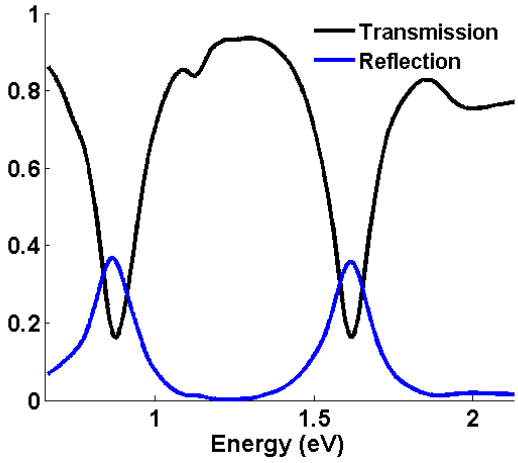

Fig. 2. Normal incidence transmission and reflection spectra for horizontal polarization.

ments [30, 40]. The topological charge is taken as $n = 1$. The peak of the electron loss occurs at 0.863 eV, or 1437 nm, which is around the magnetic resonance in Fig. 2.

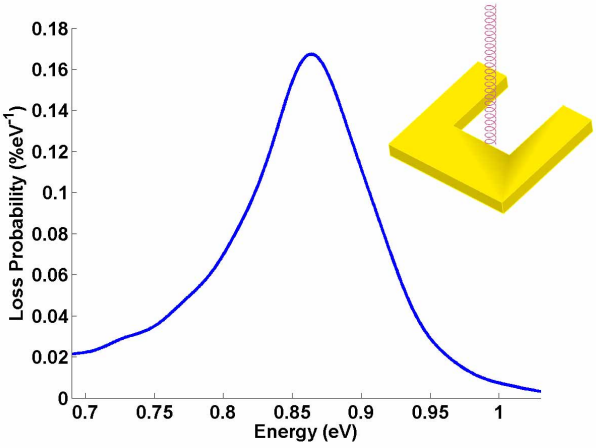

Fig. 3. Calculated vortex electron beam energy loss scattering probability of the SRR structure in Fig. 1 for 100 keV beam with transverse co-ordinate $\boldsymbol{R}_0 = (0, 90\ \text{nm})$.

Figure 4 shows the vortex-EELS probability map for the energy loss peak at 0.863 eV with a 100 keV beam. The location of the maximum scattering probability is in the middle of the SRR, close to the metal edge. An additional video (Media 1) is provided showing the evolution of the map approaching the resonance.

3.3. EELS Maps for the SRR

Figure 5 shows the conventional EELS scattering probability map of the same SRR structure for its maximum scattering loss energy of 0.8 eV. This figure was calculated using standard EELS theory [41] and by moving an electric dipole source over the trajectory of the beam. This figure is provided to show the different distribution of the EELS and vortex-EELS maps. As

#166622 - $15.00 USD Received 13 Apr 2012; revised 25 May 2012; accepted 11 Jun 2012; published 20 Jun 2012

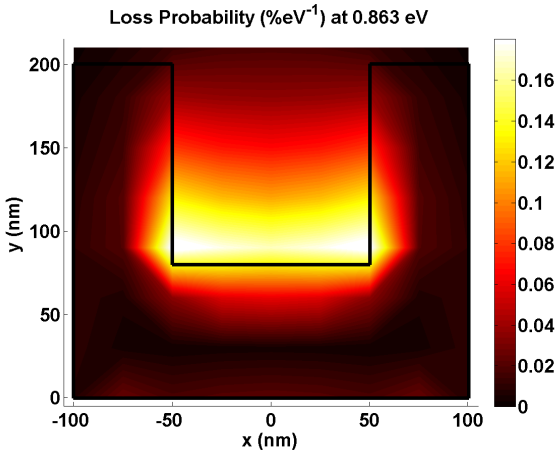

Fig. 4. Map of vortex-EELS probability as a function of position for the 0.863 eV loss peak and a 100 keV beam. A video (Media 1) showing the vortex-EELS for different loss energies is provided online.

expected, the EELS map of Fig. 5 shows the same distribution and a similar energy resonance as previously found for the lowest energy EELS spectrum for a similar SRR structure [42]. This corresponds to the lowest order plasmonic resonance [43].

For the EELS map, the maximum scattering occurs at the ends of the arms of the SRR structure. It should be noted that we have validated the quantitative EELS values provided by our calculation method by reproducing past scattering values, as shown in the Appendix. Although in many cases having a smaller mesh size will increase the accuracy of FDTD, the local density of states inside a lossy material is necessarily grid size dependent. This dependence is related to the breakdown of the dipole approximation. A physically reasonable grid size to choose then is the comparable to the size of the physical source, in this case the vortex electron beam. In this way, FDTD calculations can correctly regularize the devergent Green function due to the finite sized grid inside the lossy structure [39]. Similar techniques are commonly employed for computing the spontaneous emission rate of a photon source in a lossy medium; one must model finite size dipoles to have a meaningful (and non-divergent) answer.

4. Discussion

The most encouraging result of the calculations presented in this theoretical work is the finding that vortex-EELS is within an order of magnitude of the conventional EELS for the same structure. Since regular EELS has been used extensively to map out the electric response of metal nanoparticles, this finding is promising for the near-future use of vortex-EELS to map out the magnetic response. For the SRR, the maximum magnetic response occurs in the region of the highest magnetic field of the so-called “magnetic plasmon resonance,” which is consistent with past works on SRR structures [11].

From a theoretical point of view, the magnetic and electric Green functions are actually not independent. Indeed, they are related through the expression [44]:

$$\frac{\omega^2}{c^2}\overline{\boldsymbol{G}}^{\mathrm{H}}(\boldsymbol{r},\boldsymbol{r}',\omega) = [\nabla_{\boldsymbol{r}}\times]\cdot\overline{\boldsymbol{G}}^{\mathrm{E}}(\boldsymbol{r},\boldsymbol{r}',\omega)\cdot[\nabla_{\boldsymbol{r}'}\times]. \tag{18}$$

This relation shows that the longitudinal component of the magnetic Green function gives information about the transverse electric components. Therefore, the combination of EELS

#166622 - $15.00 USD Received 13 Apr 2012; revised 25 May 2012; accepted 11 Jun 2012; published 20 Jun 2012

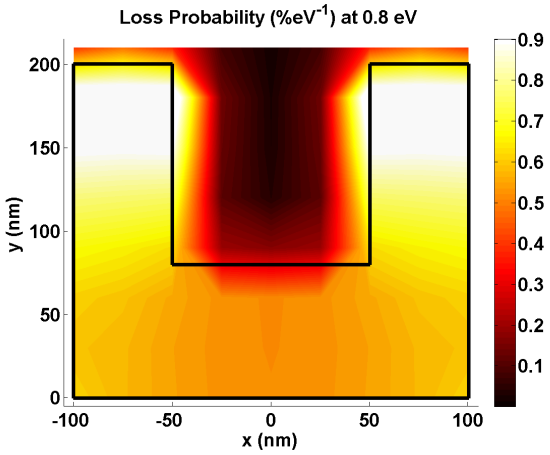

Fig. 5. Map of EELS probability as a function of position for the 0.8 eV loss energy and a 100 keV beam. A video (Media 2) showing the EELS for different loss energies is provided online.

and vortex-EELS provides a more complete picture of the electromagnetic response at the nanoscale. This picture is not entirely complete, however, due to the integration over the path of the electron beams, but it may suffice to provide greater insight for sufficiently thin and symmetric structures.

It is worthwhile to mention that the vortex electron trajectory will also have the usual electric contribution. The vortex-EELS contribution can be separated out by noting the spatial-spectral vortex-EELS response; that is, the resonances of Figs. 4 and 5 occur at different energies. Another technique would be to filter the scattered electron beam by its OAM (for example, by using diffractive or magnetic prisms) if it is has transferred OAM to the SRR, then it will no longer have OAM.

It should be noted that our calculations of vortex-EELS assumed $n = 1$ and $a = 1$ nm, which is consistent with recent experiments showing subnanometer focusing of vortex beams [45]. It is possible, however, to increase the effective magnetic charge either by increasing the topological charge n (linear dependence) or decreasing the beam size a (inverse square dependence). Since the magnetic charge is squared in the energy loss calculations, any improvements will be squared there as well. The increased n has been demonstrated in experiment [40]. It is possible that improved electron optics will lead to reduced a as well.

Finally, we comment that should vortex-EELS be successfully demonstrated, it will prove to be a powerful tool to quantify the local magnetic response of metal nanostructures. This is of interest to many applications; for example, the development of negative index metamaterials with a stronger response, a lower loss and a shorter wavelength resonance.

5. Conclusions

We have presented the theory of vortex-EELS to map out the magnetic response of a metal nanostructure at the nanometer scale. Our findings show that with reasonable parameters based on past experiments, the vortex-EELS signal from a SRR should be within an order of magnitude of conventional EELS. Since conventional EELS is performed routinely on metal nanostructures, this is a promising result for future works aimed at improving the magnetic response of metal nanostructures in the visible regime by obtaining a microscopic picture.

#166622 - $15.00 USD Received 13 Apr 2012; revised 25 May 2012; accepted 11 Jun 2012; published 20 Jun 2012

Appendix

Starting from the full Maxwell equations, assuming $\mu_r = 1$, one can show

$$\nabla \times \nabla \times \boldsymbol{E}(\boldsymbol{r},\omega) - k_0^2 \boldsymbol{\varepsilon}_r(\boldsymbol{r},\omega)\boldsymbol{E}(\boldsymbol{r},\omega) = \varepsilon_0 k_0^2 \boldsymbol{P}_e(\boldsymbol{r},\omega) = i\omega\mu_0\, \boldsymbol{j}_e(\boldsymbol{r},\omega), \tag{19}$$

where $\boldsymbol{P}_e$ and k_0 are the electric polarization and wavenumber. Using an electric-dipole polarization source in the Maxwell equations, it is easy to derive the electric-field Green function equation:

$$\nabla \times \nabla \times \overline{\boldsymbol{G}}^{\mathrm{E}}(\boldsymbol{r},\omega) - k_0^2 \boldsymbol{\varepsilon}(\boldsymbol{r},\omega)\overline{\boldsymbol{G}}^{\mathrm{E}}(\boldsymbol{r},\omega) = \varepsilon_0 k_0^2\, \delta(\boldsymbol{r}-\boldsymbol{r}'), \tag{20}$$

so that $\boldsymbol{E}(\boldsymbol{r},\omega) = \frac{1}{\varepsilon_0}\int d\boldsymbol{r}'\overline{\boldsymbol{G}}^{\mathrm{E}}(\boldsymbol{r},\boldsymbol{r}',\omega)\cdot\boldsymbol{P}_e(\boldsymbol{r}',\omega)$, is in term of the E-field current density:

$$\boldsymbol{E}(\boldsymbol{r},\omega) = \frac{i}{\varepsilon_0\omega}\int d\boldsymbol{r}'\overline{\boldsymbol{G}}^{\mathrm{E}}(\boldsymbol{r},\boldsymbol{r}',\omega)\cdot\boldsymbol{j}_e(\boldsymbol{r}',\omega). \tag{21}$$

One can also construct a wave equation for the $\boldsymbol{H}$ field:

$$\begin{aligned}\nabla \times \frac{1}{\boldsymbol{\varepsilon}_r(\boldsymbol{r},\omega)}\nabla \times \boldsymbol{H}(\boldsymbol{r},\omega) - k_0^2\boldsymbol{H}(\boldsymbol{r},\omega) &= \nabla \times \frac{-i\omega}{\boldsymbol{\varepsilon}_r(\boldsymbol{r},\omega)}\boldsymbol{P}_e(\boldsymbol{r},\omega) = \nabla \times \frac{1}{\boldsymbol{\varepsilon}_r(\boldsymbol{r},\omega)}\boldsymbol{j}_e(\boldsymbol{r},\omega)\\ &\equiv \mu_0 k_0^2 \boldsymbol{P}_m(\boldsymbol{r},\omega) \equiv i\omega\varepsilon_0\, \boldsymbol{j}_m(\boldsymbol{r},\omega),\end{aligned} \tag{22}$$

where we have introduced a magnetic-field polarization, $\boldsymbol{P}_m$, and a magnetic-field current density. Equating coefficients then gives

$$\boldsymbol{j}_m(\boldsymbol{r},\omega) = \frac{-i}{\omega\varepsilon_0}\nabla \times \frac{1}{\boldsymbol{\varepsilon}_r(\boldsymbol{r},\omega)}\boldsymbol{j}_e(\boldsymbol{r},\omega). \tag{23}$$

This gives Eq. (3). Note that the k_0^2 difference between Eq. (16) and Eq. (22) requires suitable normalization of dipole source in calculations. We choose a different form for Eq. (16) since it is more conventional.

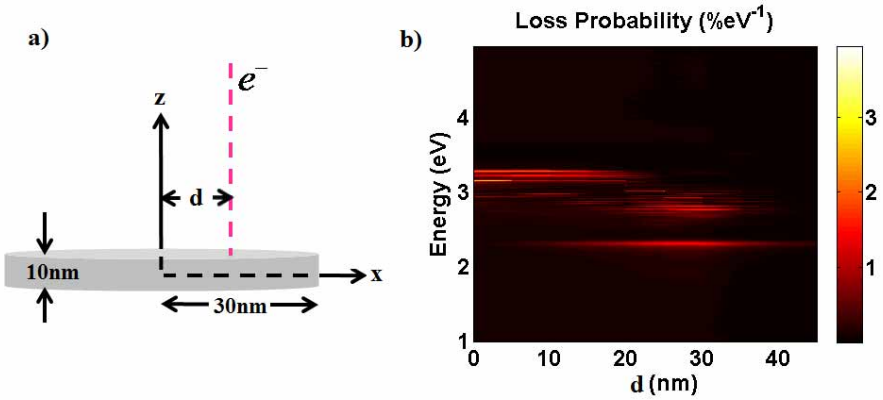

Fig. 6. (a) Schematic of silver disk, (b) Electron energy loss scattering probability for a silver disk, for comparison with Fig. 2(e) of Ref. [33].

We have repeated past calculation of EELS scattering by a silver disk for 100 keV beam to ensure that our numerical procedure was giving good quantitative agreement with those

#166622 - $15.00 USD Received 13 Apr 2012; revised 25 May 2012; accepted 11 Jun 2012; published 20 Jun 2012

works [33]. The FDTD parameters chosen were the same as those in Section 3.3. Figure 6 (a) shows a schematic of the disk structure. Figure 6 (b) shows the scattering probability as a function of energy and the radial displacement. These results are close to those found in a past work using the boundary element method [33]. In particular, the scattering probability of the peak at 2.5 eV is 2%/eV (close to edge of disk), and the scattering probability of the peak at 3.4 eV is 2%/eV, whereas the values found in that past work were around 2.5%/eV.

Acknowledgments

This work was supported by a National Sciences and Engineering Research Council of Canada (NSERC) Strategic Project Grant.

#166622 - $15.00 USD Received 13 Apr 2012; revised 25 May 2012; accepted 11 Jun 2012; published 20 Jun 2012